Metrologia

Novel developments of refractive power measurement techniques in the automotive world

OPEN ACCESS
IOP Publishing | Bureau International des Poids et Mesures Metrologia
Metrologia **60** (2023) 064001 (14pp) https://doi.org/10.1088/1681-7575/acf1a4

Novel developments of refractive power measurement techniques in the automotive world

Dominik Werner Wolf[1,2,*], **Markus Ulrich**[2] **and Alexander Braun**[3]

[1] Glass Laboratory of the Volkswagen Group, Wolfsburg, Germany
[2] Machine Vision Metrology, Institute of Photogrammetry and Remote Sensing (IPF), Karlsruhe Institute of Technology (KIT), Karlsruhe, Germany
[3] Department of Electrical Engineering, University of Applied Sciences Düsseldorf (HSD), Düsseldorf, Germany

E-mail: dominik.werner.wolf@volkswagen.de and dominik.wolf@partner.kit.edu

Received 13 January 2023, revised 14 August 2023
Accepted for publication 18 August 2023
Published 25 September 2023

Abstract

Refractive power measurements serve as the primary quality standard in the automotive glazing industry. In the light of autonomous driving new optical metrics are becoming more and more popular for specifying optical quality requirements for the windshield. Nevertheless, the link between those quantities and the refractive power needs to be established in order to ensure a holistic requirement profile for the windshield. As a consequence, traceable high-resolution refractive power measurements are still required for the glass quality assessment. Standard measurement systems using Moiré patterns for refractive power monitoring in the automotive industry are highly resolution limited, wherefore they are insufficient for evaluating the camera window area. Consequently, there is a need for more sophisticated refractive power measurement systems that provide a higher spatial resolution. In addition, a calibration procedure has to be developed in order to guarantee for the comparability of the measurement results. For increasing the resolution, a measurement setup based on an auto-correlation algorithm is tested in this paper. In order to benchmark the proposed high-resolution refractive power measurement technique, a novel laser-based setup has been realized in the Volkswagen Laser Laboratory as a reference method tuned for high-accuracy measurements. Furthermore, a calibration procedure is established by using a single reference lens with a nominal refractive power of 100 km^{-1}. For the calibration of the entire measurement range of the system, the lens is tilted by an inclination angle orthogonal to the optical axis. The effective refractive power is then given by the Kerkhof model. By adopting the measurement and calibration procedure presented in this paper, glass suppliers in the automotive industry will be able to detect relevant manufacturing defects within the camera window area more accurately paving the way for a holistic quality assurance of the windshield for future advanced driver-assistance system (ADAS) functionalities. Concurrently, the traceability of the measurement results is ensured by establishing a calibration chain based on a single reference lens, which is traced back to international standards.

* Author to whom any correspondence should be addressed.

Keywords: automotive optical quality testing, refractive power and Fourier optics, refractive power measurement methods, measurement uncertainty (GUM), Kerkhof model, deep optics, uncertainty quantification and propagation

(Some figures may appear in colour only in the online journal)

1. Introduction

In the light of the ambition to launch level 4 [1] ready autonomous driving vehicles within this decade, car manufacturers have to face completely new challenges. According to the SAE International Standard J3016-202 104 [1], level 4 driving is given if the driver becomes a passenger who can request manual control if desired or needed. The latter statement is applicable if the functionality is limited to specific terrains or external conditions. In this case, the driver will be asked to take over but the car has to be able to fall back to a minimal risk condition automatically. Developing a robust level 4 systems is quiet complex. For example, in order to guarantee that the perception latency is always smaller than the maximum reaction time to avoid a collision, level 4 ready cars will need higher spatial resolution cameras for the frontal far field [2]. This triggers higher quality requirements for the car windshield since the sensitivities for optical aberrations are amplified by using telephoto lenses. One way to assess the optical quality of a system is given by evaluating the refractive power. The high pixel resolution per field angle of telephoto cameras makes it necessary to develop high spatial resolution measurement methods for analyzing the refractive power distribution within the windshields camera window. From an economic perspective, the inspection of the compliance of technical parts should be achieved on a high confidence to minimize the number of unrectifiable rejects. Consequently, a detailed uncertainty analysis for every measurement method is mandatory to qualify these systems for industrial quality inspection. Furthermore, in a highly globalized industrial sector like the automotive branch it is of paramount importance that different methods yield the same result. In general, there are three fundamental pillars for a valid measurement in metrology, namely reproducibility, comparability and traceability. The reproducibility quantifies the degree of agreement between the measurement results of experiments conducted at locations with different environmental conditions, different instrumentation, different parameterisation or different experimenter but the measurement method remains unaffected. The comparability assesses the degree of agreement between different measurements methods or principles. The traceability is essential for establishing a calibration chain and to trace back the measurement results to international standards. In other words, the reproducibility, comparability and traceability of the measurement results has to be demonstrated in order to guarantee for the scalability of industrial solutions and applications in a globalized world. Typically, the comparability is established by a round robin test including different laboratories. The reference object under test is usually a primary standard and the entire measuring range can be tested by exploiting natural laws as a baseline model.

In this paper, we introduce three different approaches to measure the refractive power of windshields. First of all, a conventional refractive power measurement setup based on Moiré interference patterns is presented, which is currently the standard measurement technique in automotive quality testing [3, 4]. Secondly, a new high spatial resolution refractive power measurement technique is introduced based on background oriented Schlieren (BOS) imaging [5]. Finally, an experimental reference setup has been developed to provide an additional metrological baseline tuned for high accuracy measurements. For this method, we work out the uncertainty budget in great detail based on the Guide to the Expression of Uncertainty in Measurement (GUM) [6]. Furthermore, this paper investigates the comparability of the presented measurement methods based on the Kerkhof model [7], which characterises the amplification of the refractive power of a lens if a tilt angle is applied. To justify the validity of this procedure, the inherent assumptions of the Kerkhof model are worked out in detail by deriving the governing equations in section 2. The approximations which are made in order to get a spatially independent amplification factor for the refractive power results in model limitations. Those limitations of the Kerkhof model are studied in section 2.1 and determine the scope of the model validity. In section 3, we introduce the aforementioned measurement methods regarding the refractive power and the comparability study based on the Kerkhof model is presented in section 4. In addition, the link between refractive power and Fourier optics is worked out in section 5 to give an outlook on how optical quality requirements for level 4 driving functionalities could be tested in future. Section 6 concludes the results of this paper and motivates further research activities.

2. Surface imperfections of plane parallel glasses

In this section, we analyze the impact of surface imperfections on the ray propagation. The equations, which we derive by utilizing the concept of ray optics, have already been presented by Schardin and Stamm [8] and Kerkhof [7]. Nevertheless, it is important to recall the underlying physical assumptions in order to understand the full picture behind the governing DIN-52 305 industrial standard [4]. Figure 1 shows a sketch of a glass plate perturbed by surface imperfections. The angles can be derived by geometrical considerations and are given by equations (1)–(5). In addition, Snell's law is adapted for the ray transition from air ($n_{\text{air}} \approx 1$) to glass ($n_{\text{glass}} \approx 1.52 =: n$) and vice versa. The general idea of the Kerkhof model is to treat the perturbations of a glass plate as local prisms. Hence, the surface perturbations of the glass are translated into a map of prism wedge angles $\delta(x,y)$. For simplification, the

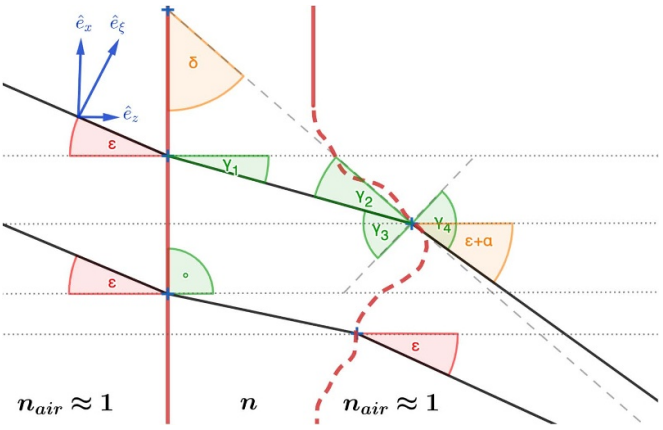

Figure 1. Sketch of a plane parallel glass plate (red line) perturbed by surface imperfections (dashed red line). The incoming collimated beam (black line) is refracted by surface imperfections leading to a local focus effect.

two-dimensional problem is studied on the condition $y \stackrel{!}{=} 0$ without loss of generality. The analysis of figure 1 results in the following algebraic angular relationships:

$$\sin\epsilon = n \cdot \sin\gamma_1 \,, \tag{1}$$

$$\gamma_2 = \frac{\pi}{2} - \delta - \gamma_1 \,, \tag{2}$$

$$\gamma_3 = \frac{\pi}{2} - \gamma_2 \,, \tag{3}$$

$$n \cdot \sin\gamma_3 = \sin\gamma_4 \,, \tag{4}$$

$$\epsilon + \alpha = \gamma_4 - (\gamma_3 - \gamma_1) \,. \tag{5}$$

The equations from expression (1)–(5) can be used to derive the deflection angle α as a function of the wedge angle δ. The mathematical relationship is derived subsequently in Expression (6):

$$\begin{aligned}
\epsilon + \alpha &\stackrel{(5,4,3)}{=} \arcsin\left(n \cdot \sin\gamma_3\right) - \left(\frac{\pi}{2} - \gamma_2 - \gamma_1\right) \\
\Leftrightarrow \epsilon + \alpha &\stackrel{(3,2)}{=} \arcsin\left(n \cdot \cos\gamma_2\right) - \delta \\
\Leftrightarrow \epsilon + \alpha + \delta &\stackrel{(2,1)}{=} \arcsin\left(n \cdot \sin\left(\arcsin\left(\frac{\sin\epsilon}{n}\right) + \delta\right)\right) \\
\Leftrightarrow \sin\left(\epsilon + \alpha + \delta\right) &= n \cdot \sin\left(\arcsin\left(\frac{\sin\epsilon}{n}\right) + \delta\right) \\
\Leftrightarrow \sin\left(\epsilon + \alpha + \delta\right) &= \sin\epsilon \cdot \cos\delta + n \cdot \cos\left(\arcsin\left(\frac{\sin\epsilon}{n}\right)\right) \cdot \sin\delta \\
\Leftrightarrow \sin\left(\epsilon + \alpha + \delta\right) &= \sin\epsilon \cdot \cos\delta + \sqrt{n^2 - (\sin\epsilon)^2} \cdot \sin\delta \\
\Leftrightarrow \sin\left(\epsilon + \alpha + \delta\right) &= \sin\epsilon + \delta \cdot \sqrt{n^2 - (\sin\epsilon)^2} + \mathcal{O}\left\{\delta^2\right\} \,.
\end{aligned} \tag{6}$$

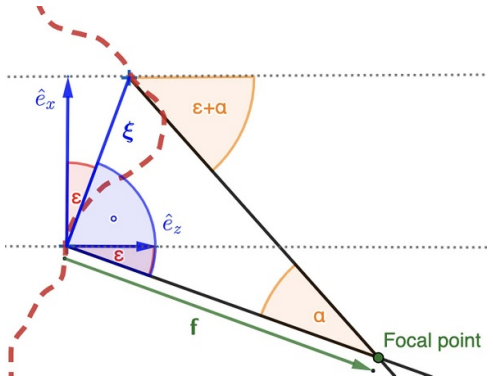

Figure 2. The local deflection angle α can be related to a local refractive power distortion D with focal length f.

It is important to emphasize that the wedge angle δ quantifies the local imperfections of the glass surface and has an implicit spatial dependency. The deflection angle α is amplified if the optical system is tilted by the inclination angle ϵ. At this point, the assumption is made that the local wedge angle δ is small ($\delta \ll \frac{\pi}{4}$) and that the deflection angle α is small as well ($\alpha \ll \frac{\pi}{4}$). Hence, expression (6) can be further simplified as demonstrated in expression (7):

$$\begin{aligned}
&\sin\left(\epsilon + \alpha + \delta\right) = \sin\left(\epsilon + \alpha\right) \cdot \cos\delta + \cos\left(\epsilon + \alpha\right) \cdot \sin\delta \\
\Leftrightarrow\ &\sin\left(\epsilon + \alpha + \delta\right) = \sin\epsilon \cdot \cos\alpha \cdot \cos\delta + \cos\epsilon \cdot \sin\alpha \cdot \cos\delta \\
&\qquad + \cos\epsilon \cdot \cos\alpha \cdot \sin\delta - \sin\epsilon \cdot \sin\alpha \cdot \sin\delta \\
\Leftrightarrow\ &\sin\left(\epsilon + \alpha + \delta\right) = \sin\epsilon \cdot \cos\alpha + \cos\epsilon \cdot \sin\alpha + \delta \cdot \cos\epsilon \cdot \cos\alpha \\
&\qquad - \delta \cdot \sin\epsilon \cdot \sin\alpha + \mathcal{O}\left\{\delta^2\right\} \\
\Leftrightarrow\ &\sin\left(\epsilon + \alpha + \delta\right) = \sin\epsilon + \alpha \cdot \cos\epsilon + \delta \cdot \cos\epsilon - \alpha \cdot \delta \cdot \sin\epsilon \\
&\qquad + \mathcal{O}\left\{\delta^2\right\} + \mathcal{O}\left\{\alpha^2\right\} \\
\Leftrightarrow\ &\sin\left(\epsilon + \alpha + \delta\right) = \sin\epsilon + \alpha \cdot \cos\epsilon + \delta \cdot \cos\epsilon + \mathcal{O}\left\{(\alpha + \delta)^2\right\} \,.
\end{aligned} \tag{7}$$

Due to the small-angle approximation, higher order terms $\mathcal{O}$ can be neglected. As a consequence, in first order approximation the deflection angle α is given by expression (8):

$$\begin{aligned}
\sin\epsilon + \alpha \cdot \cos\epsilon + \delta \cdot \cos\epsilon &\stackrel{(6)}{\approx} \sin\epsilon + \delta \cdot \sqrt{n^2 - (\sin\epsilon)^2} \\
\Leftrightarrow \alpha &\approx \delta \cdot \left[\frac{1}{\cos\epsilon} \cdot \sqrt{n^2 - (\sin\epsilon)^2} - 1\right] \quad \blacksquare \,.
\end{aligned} \tag{8}$$

Equation (8) determines the relationship between the local deflection angle $\alpha(x)$ and the local wedge angle $\delta(x)$. The local deflection angle can be translated to a local refractive power of

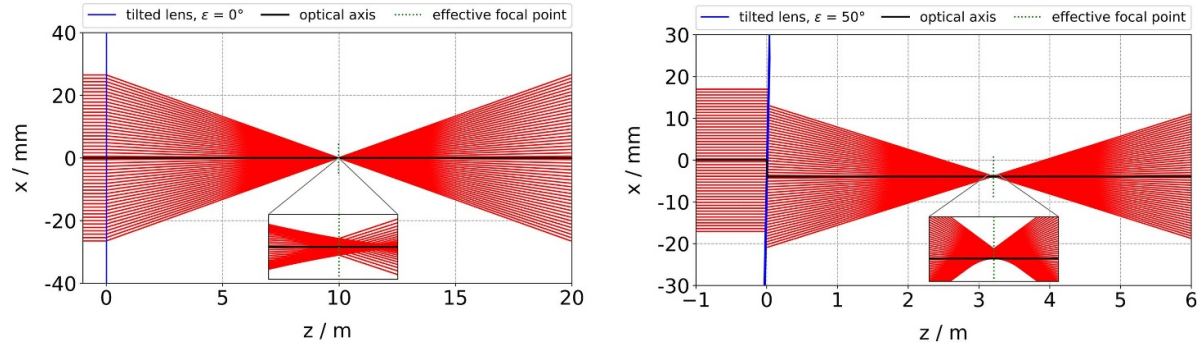

Figure 3. Ray tracing simulation for the laser setup at an angle of $\epsilon = 0°$ (left) and $\epsilon = 50°$ (right). The parameterisation of the simulation is defined by the measurement setup described in section 3.3.

the glass. This is illustrated in figure 2 and can mathematically be described by utilizing the sine rule as demonstrated by the subsequent equations (9)–(11):

$$D := \frac{\partial \alpha}{\partial \xi} = \frac{\partial \alpha}{\partial \delta} \cdot \frac{\partial \delta}{\partial x} \cdot \frac{\partial x}{\partial \xi} =: \frac{1}{f}\,, \tag{9}$$

$$\frac{x}{\xi} = \frac{\sin\left(\frac{\pi}{2} + \alpha\right)}{\sin\left(\frac{\pi}{2} - \alpha - \epsilon\right)} = \frac{\cos\alpha}{\cos\left(\alpha + \epsilon\right)} \approx \frac{1}{\cos\epsilon}\,, \tag{10}$$

$$D_\epsilon \overset{(8,9,10)}{\approx} \frac{1}{\cos\epsilon} \cdot \left[\frac{1}{\cos\epsilon} \cdot \sqrt{n^2 - (\sin\epsilon)^2} - 1\right] \cdot \frac{\partial \delta}{\partial x}\,. \tag{11}$$

In general, the refractive power quantifies the first derivative of the local deflection angle α with respect to the orthogonal off-axis coordinate ξ. The spatial dependency in equation (11) on the wedge angle profile can be eliminated if the ratio to the on-axis case is considered ($\epsilon = 0°$). The resulting amplification factor for the refractive power of the perturbed glass depends exclusively on the inclination angle ε:

$$\frac{D_\epsilon}{D_0} \overset{(11)}{\approx} \frac{1}{(n-1)\cdot\cos\epsilon} \cdot \left[\frac{1}{\cos\epsilon} \cdot \sqrt{n^2 - (\sin\epsilon)^2} - 1\right] \quad \blacksquare\,. \tag{12}$$

As a result, equation (12) paves the way for calibrating refractive power measurement devices over the entire range based on a single reference lens. By tracing back the reference lens to international standards we can safeguard the validity of the calibration strategy and ensure that the fundamental traceability requirement for a valid measurement in metrology is fulfilled.

2.1. Limitations of the Kerkhof approximation

The assumption of the Kerkhof model, given by equation (12), requires plane parallel glass. Nevertheless, the Kerkhof model can be utilised to estimate the expected refractive power of a weak focusing lens. In order to quantify the deviation from the Kerkhof model and to derive an approximation threshold for a weak focusing lens of $\langle D \rangle = 100\,\mathrm{km}^{-1}$ we implemented a ray tracing simulation in Python. As an example, figure 3 shows an ensemble of light rays refracted by the weak focusing lens under different inclination angles ϵ. The point of least confusion determines the focal length of the lens for the corresponding inclination angle.

As a side effect, the circle of least confusion increases as the inclination angle increases, which would result in an effective blurring if an imaging system is considered. This blurring can be quantitatively characterized by the modulation transfer function (MTF) as discussed in section 5. In addition to the inclination angle ϵ, there are two parameters that influence the effective refractive power of the lens. First of all, the thickness of the lens d_{lens} has an impact because the lens surface is curved. Secondly, the wedge angle δ has to be small, such that second order terms in δ are negligible. The three dependencies were studied in detail by executing the ray tracing simulation for different parameter settings. Figure 4(a) demonstrates that the systematic bias between Kerkhof model and physical simulation is less than 0.5% for $\epsilon \leqslant 70°$. Typically, car windshields are inclined by less than $\epsilon = 70°$, wherefore the Kerkhof model is sufficiently accurate for the scope of car windshield measurements. The thickness of the reference lens, produced and calibrated by ZEISS, is given by $\langle d_{lens} \rangle = 10.1\,\mathrm{mm}$. Thicknesses of up to 40 mm result in systematic biases of less than 1% according to figure 4(b). The wedge angle for the spherical lens is not constant over the entire profile of the aperture surface. Therefore, the maximum wedge angle δ was varied, which corresponds to different maximum aperture diameters. From figure 4(c) can be concluded, that the maximum aperture stop of the reference lens, which corresponds to a maximum wedge angle of $\delta = 4.7\,\mathrm{mrad}$, does not violate the assumptions of the Kerkhof model. Hence, the measurement bias is much smaller than 1% for a maximum inclination angle of $\epsilon = 70°$. In conclusion, the Kerkhof model is valid within the refractive power measurement range of weak focusing lenses. Consequently, by periodically recalibrating the reference lens, refractive power measurement systems can be traced back to international standards and national metrological institutes, e.g. PTB, METAS, NIST.

3. Refractive power measurement methods

3.1. Moiré interference method

A very well-established refractive power measurement technique in the automotive industry is based on Moiré

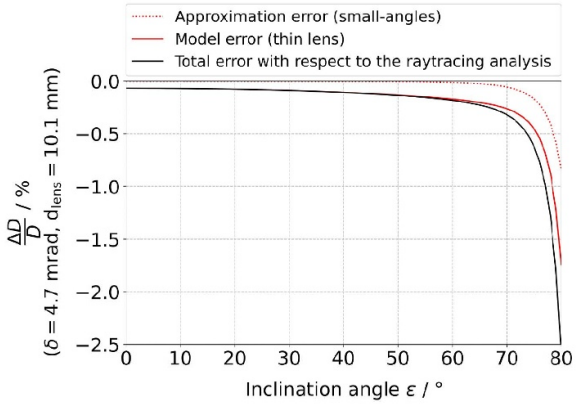

(a) Exact solution versus first order, small angle approximation.

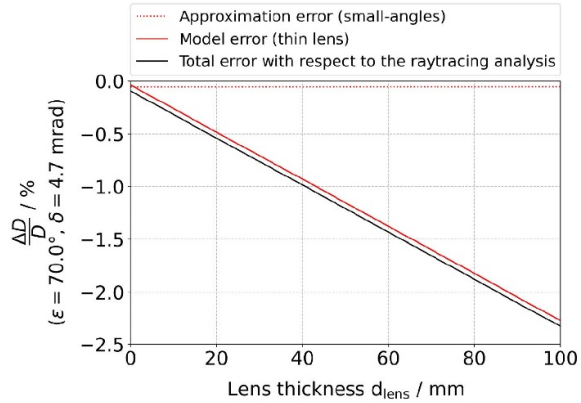

(b) Impact of lens thickness.

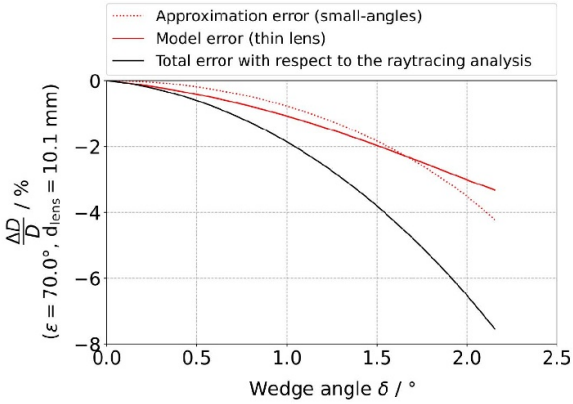

(c) Wedge angle dependency.

Figure 4. Robustness analysis of the Kerkhof model. For the parameterisation of the simulation, the worst case scenario has been considered. The worst case scenario is given by the edge of the reference lens aperture (aperture edge corresponds to a wedge angle of $\delta = 4.7\,\text{mrad}$) and the maximum test angle of $\epsilon = 70°$.

interference patterns [9–11]. Initially, a fine-line grid is illuminated by a coherent light source. The grid pattern is then propagated through the windshield and mapped onto a secondary line grid with a rotational offset. Without any optical perturbations of the windshield, the superposition of the line grid patterns creates a Moiré interference pattern with constant differentiation length l_0. Due to surface imperfections, optical aberrations will perturb the transmitted line grid pattern and the superposition of the perturbed and unperturbed pattern will show local deviations from the constant differentiation length l_0. The deviation from the differentiation length Δl_0 gives rise to the local deflection angle of the light beam induced by the windshield. By differentiating the deflection angle profile along the horizontal and vertical dimension, the refractive power map is retrieved. The resolution of the system is limited by the differentiation length l_0, which is problematic for investigating small camera areas of advanced driver-assistance system (ADAS) cameras.

3.2. *Auto-correlation method*

The local refractive power is mathematically defined as the first derivative of the deflection angle (see equation (9)). This gives rise to a new measurement approach based on BOS imaging [5, 12–14]. If the image of a reference pattern is taken by a camera with and without the windshield in the optical path (as visualized in figure 5), then a map of local deflection angles can be reconstructed based on the structure of the perturbed reference pattern by an auto-correlation algorithm. The local deflection angles are determined by the ratio of the corresponding deflection vector component related to the optical path length (as shown in figure 6). Consequently, a local refractive power map can be calculated by numerical differentiation, which results in an uniform refractive power distribution in case of the reference lens since the slopes in figure 6 are location-independent. The last step is a bit more complex than described because the optical parameters of the setup have to be considered for an accurate result. For this, the target vector is mapped by a matrix optics approach onto the image plane. Consequently, this measurement setup implicitly assumes the validity of the small angle approximation, which breaks down for severe optical distortions. Nevertheless, for the scope of optical distortions in automotive applications, where D is much smaller than $1\,\text{m}^{-1}$, the assumption is valid. In addition, the mapping approximates the camera system as a pinhole camera and the distances between the optical

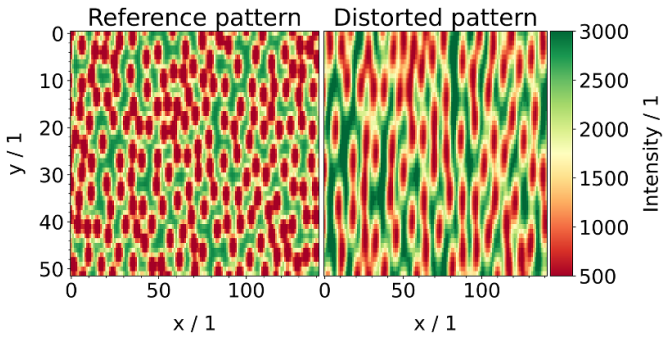

Figure 5. The reference pattern and the distorted pattern is visualized for the reference lens under a test angle of $\epsilon = 59.7°$. It is clearly noticeable, that the circular reference pattern is distorted towards elliptical shapes due to the broken symmetry as a consequence of the inclination angle, which induces an amplification factor in this direction according to the Kerkhof model.

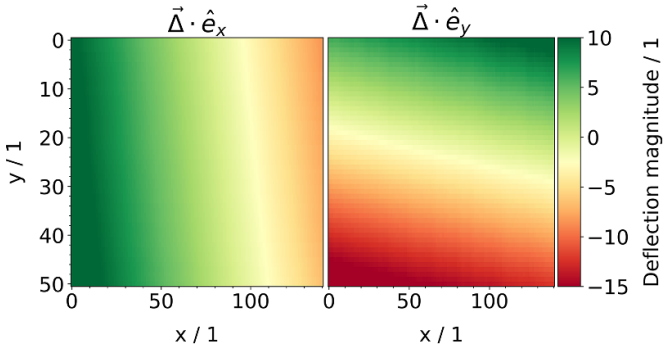

Figure 6. The horizontal and the vertical component of the deflection vector $\vec{\Delta}$ is shown for the reference lens under a test angle of $\epsilon = 59.7°$. The homogeneity of the slopes indicates an uniform refractive power distribution. The mean refractive power value of the reference lens over the aperture surface amounts to $D_{\text{meas}} = 577\,\text{km}^{-1}$.

elements are determined by a camera calibration procedure. Unfortunately, a more detailed description of those steps can not be given due to confidentiality obligations. The major advantage of this technique lies in the degree of freedom of choosing an arbitrary axis of interest for the refractive power calculation. Furthermore, the resolution of the system is only limited by the areal density of the reference pattern, which is subject to the magnitude of the distortion. Basically, if the distortions are severe (like in figure 5), then the areal density has to be high enough, so that the auto-correlation algorithm can still identify enough reference points on the target for a given subset size. On the other hand, the areal density has to be low enough in order to guarantee for the discriminability of the reference points within the pattern. Finally, it has to be emphasized, that the auto-correlation measurement technique regarding the refractive power is still subject to ongoing research. We address some of the unresolved issues in more detail in section 4.

3.3. Laser-based method

As a reference setup for refractive power measurements, a laser-based method has been realized in the Volkswagen Laser Laboratory. The setup is presented in figure 7 and is advertised as a reference measurement method because of the high measurement accuracy, which is achieved by operating the experimental setup at a smooth region of the multidimensional target function (14) leading to small sensitivity coefficients. This procedure is only possible if an excellent parameterability of the experimental setup is given. On the downside, the laser measurement setup is characterized by the worst spatial resolution of the studied methods, wherefore it would be inadequate for automotive applications. Consequently, the following considerations serve exclusively the intention to provide an experimental method for determining the ground truth refractive power.

The principle idea of the measurement setup is to observe the transversal distance between two laser beams after passing a refractive element as proposed by §9.2.1.1.3 of the UN/ECE-R43 regulation on safety glasses [15]. For the experimental setup, a photonic beam is generated by a laser. The beam is attenuated and multiplied by a crystal beam splitter. The outgoing laser beams are parallelized by the method of superimposition with an alignment mirror. At the end of the optical table, the beams are separated by a distance of $\mu_0 = (53.0 \pm 0.5)\,\text{mm}$. The observation plane is located in a distance of $L = (20.65 \pm 0.02)\,\text{m}$. Even though the alignment procedure was executed with much care, the initial laser beam and the spatially conjugated beam are in practice not perfectly congruent. For that reason, the divergence angle α_0 of the measurement setup has to be determined. The divergence angle is specified by the transversal distance reduction over the optical axis coordinate z. If the transversal distance of $\tau_0 = (38.4 \pm 0.5)\,\text{mm}$ between the laser beams is

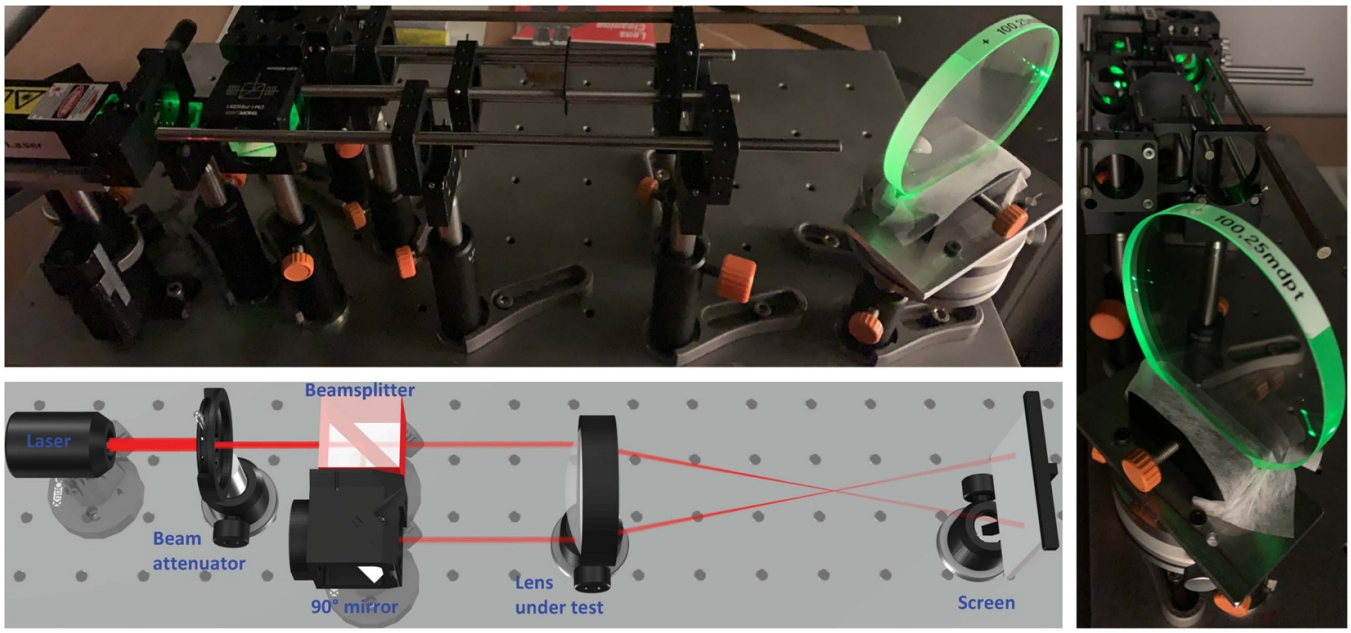

Figure 7. Laser measurement setup for measuring the refractive power as a function of the inclination angle. Upper Left: cross-section view of the optic board. Lower left: Schematic drawing of the laser light path. Right: head-on view of the optic board. Please note: The schematic drawing is not equidistantly representing the real alignment distances. The lens is mounted on a pivot bearing with an alignment tolerance of $\sigma_\epsilon = 30.6''$, which is sufficiently precise in order to neglect this uncertainty contribution.

measured in the observation plane, without a refracting sample inside the light path, then the divergence angle α_0 is given by equation (13):

$$\tan\alpha_0 := \frac{\tau_0 - \mu_0}{2L} \quad \Rightarrow \quad \alpha_0 \approx \frac{\tau_0 - \mu_0}{2L} \approx -1.22' \,. \tag{13}$$

The particular choice of the parameterisation results from a trade-off between the goal of operating at an optimal working point characterized by small sensitivity coefficients and the practical limitations of the alignment parameters given by the spatial dimensions of the laser laboratory and the optic board respectively. The corresponding measurement uncertainties of the alignment parameters are given by the specifications of the measurement rulers on a confidence level of 68.3% assuming a Gaussian distribution ($k = 1$).

For the propagation of the laser beams along the optical axis, the matrix optics formalism can be deployed. This formalism exploits the paraxial approximation and manifests a state vector $\vec{\eta}$ consisting of the transversal coordinate and the deflection angle in the corresponding plane. The state vector $\vec{\eta}_f$ in the observation plane can be determined by propagating the initial state vector $\vec{\eta}_i$ through the lens and the drift space towards the observation plane, as elaborated in detail in equation (14):

$$\begin{aligned}
\vec{\eta}_f &:= \begin{bmatrix} -\frac{d_c}{2} \\ \alpha_f \end{bmatrix} = \mathcal{M}_{\text{drift}} \cdot \mathcal{M}_{\text{lens}} \cdot \vec{\eta}_i \\
\Leftrightarrow \vec{\eta}_f &= \begin{bmatrix} 1 & L \\ 0 & 1 \end{bmatrix} \cdot \begin{bmatrix} 1 & 0 \\ -D_{\text{eff}} & 1 \end{bmatrix} \cdot \begin{bmatrix} \frac{\mu_0}{2} \\ \alpha_0 \end{bmatrix} \\
\Leftrightarrow \vec{\eta}_f &= \begin{bmatrix} \frac{\mu_0}{2} - \frac{L\mu_0 D_{\text{eff}}}{2} + L\alpha_0 \\ -\frac{\mu_0 D_{\text{eff}}}{2} + \alpha_0 \end{bmatrix} \\
\Rightarrow -\frac{d_c}{2} &\overset{(13)}{=} \frac{\mu_0}{2} - \frac{L\mu_0 D_{\text{eff}}}{2} + \frac{\tau_0 - \mu_0}{2} \\
\Leftrightarrow D_{\text{eff}} &= \frac{d_c + \tau_0}{\mu_0 L} \,.
\end{aligned} \tag{14}$$

According to equation (14), the effective refractive power of the lens is fully determined by the transversal distance d_c between the laser beam centroids. In order to measure d_c, a picture of the observation plane is taken by a Nikon D5100 with 16.2 Mpx. The horizontal distance x between the beam centroids was measured in an unbiased way, so that the refractive power calculation is not affected. In order to satisfy this condition, the camera has been positioned slightly above the optical axis, in the middle of the two beam centroids. This generated a slight skewness of the vertical intensity distributions towards larger values of y, which corresponds to the inclination angle of the camera. The image is post-processed by a Python algorithm to extract the coordinates of the beam centroids by the mode value of the intensity profile distributions. This method is used because of the non-zero skewness of the vertical intensity distributions, which would bias the estimators of a Gaussian fit in comparison. Furthermore, the upper edge of the target screen causes a sudden drop of the Fresnel reflection coefficient in the target plane, which influences the tails of the vertical profile intensity distributions. As an example, the raw image and the corresponding profile intensity distributions are presented in figure 8 for the setup at an angle of $\epsilon = 50°$. The mapping from pixel to metric coordinates is determined by a calibration factor, which was determined by an initial image of a straightedge in the region of interest on the image plane.

3.3.1. Uncertainty analysis. The uncertainty analysis is based on GUM [6]. A-priori uncertainty distributions are assigned to the input parameters by scientific judgement. The

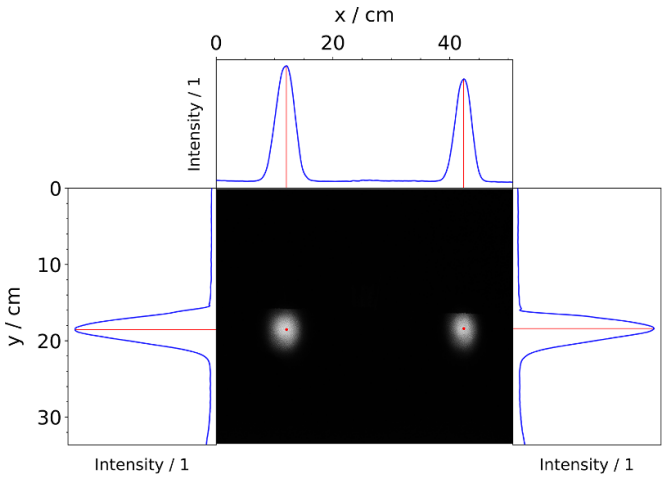

Figure 8. The raw image of the laser beam in the target plane is shown for the setup under an angle of $\epsilon = 50°$.

impact of the input variances on the target quantity is determined by Gaussian error propagation [16]. The random variables sampled from the distributions of the input quantities x_i are assumed to be uncorrelated [6], wherefore the expectation value of products factorizes: $\mathbf{E}[x_i x_j] = \mathbf{E}[x_i] \cdot \mathbf{E}[x_j]$. Consequently, the error propagation is given by the quadratic mean of the input uncertainties σ_i weighted by the sensitivity coefficients $\partial_{x_i}\mathrm{D}$ and normalised by ξ_i. The normalisation ξ_i is applied in order to unify the confidence intervals of the input uncertainties σ_i on a 68.3% confidence level. For the evaluation of the confidence level covered by the combined standard deviation σ_{eff}, the degrees of freedom of the input variances have to be determined. This is elaborated in detail in subsection 3.3.1.1 in order to guarantee the reproducibility of the resulting uncertainty budget. In general, the normalized distribution of the target quantity follows a student's t-distribution if the standard deviation is estimated and the number of degrees of freedom is small. Finally, a sophisticated uncertainty budget for the laser-based refractive power measurement method is presented in subsection 3.3.1.2.

3.3.1.1. Degrees of freedom (DoF). First of all, it is important to recapitulate, that the assigned probability density function (pdf) describes the distribution of x_i and the input uncertainty σ_x characterizes the variability or the width of the pdf. The sample standard deviation σ_{s}, defined by equation (15):

$$\sigma_{\mathrm{s}} := \sqrt{\frac{\sum_{i=1}^{N}\left(x_i - \mathbf{E}[x_i]\right)^2}{\nu}} \overset{\text{static}}{=} \sqrt{\frac{\sum_{i=1}^{N}\left(x_i - \mu\right)^2}{N-1}}\,,$$
$$\text{with:}\quad \mu := \frac{1}{N}\sum_{i=1}^{N} x_i\,, \tag{15}$$

represents an unbiased estimator for the true standard deviation σ_x if and only if the observables x_i are Gaussian distributed. According to Cochran's theorem [17], the sample variance σ_{s}^2 of the population follows a χ_ν^2-distribution of ν degrees of freedom if the deviations are independent and Gaussian distributed. The number of degrees of freedom of the residuals for an ensemble of N observations is given by $\nu = N - p$, where p corresponds to the number of independent linear constraints on the residuals and the sample variance respectively [18]. In zeroth order, the residual sum is minimized by choosing an appropriate estimator μ that fulfills the constraint $\partial_\mu \sigma_{\mathrm{s}}^2 \overset{!}{=} 0$. The estimator μ is commonly known as the arithmetic mean. If a subset from the ensemble of cardinality N is drawn, $(N-1)$ subsamples can be drawn arbitrarily but the last subsample is then fully determined by the constraint imposed by the ensemble average μ. This reduction in degrees of freedom of the sample variance is commonly addressed by the Bessel's correction factor [19]. Similar considerations can be made for non-static models, where regression is the mean of choice. If the ensemble follows an underlying linear drift, then the dynamic behavior is characterized by two parameters. The conditional equation for the slope m and the y-intercept b impose two constraints on the residuals, namely $\partial_m \sigma_{\mathrm{s}}^2 \overset{!}{=} 0$ and $\partial_b \sigma_{\mathrm{s}}^2 \overset{!}{=} 0$. In this context, σ_{s}^2 is the first order variance, where $\mathbf{E}[x_i]$ is replaced by the corresponding expectation value of the regression line. Therefore, σ_{s} quantifies the ensemble spread around the regression line in this case, which is more commonly known as the root-mean-square error (RMSE) [19]. Each parameter of the regression function needs to fulfill all constraints on the residual sum. As a consequence, the degree of freedom of the variance of each regression parameter is given by $(N-2)$ for linear cases, which also applies to the higher order variance or RMSE. The idea of higher order variances is quite useful for benchmarking regression models because minimizing the residuals by more complex models reduces simultaneously the degrees of freedom of the variance, which acts as a penalty for more complex models like in Ridge regression [20]. Consequently, the zeroth order sample variance is a benchmark for the RMSE of a regression model because the predictions have to outperform the naive estimate given by the arithmetic mean. Hence, the RMSE should reduce the randomness of the ensemble better than the zeroth order sample variance [21].

On the contrary, if only a single measurement with a-priori pdf is considered, the number of degrees of freedom for the distribution of the variance σ_s^2 has to be determined differently. In general, ν quantifies all statistical moments of the χ^2_ν-distribution, wherefore the shape of the distribution is exclusively determined by the number of degrees of freedom [19]. In the limit of $\nu \mapsto \infty$, the χ^2_ν-distribution equals a Gaussian distribution according to the central limit theorem [22]. For the purpose of uncertainty quantification and propagation, the standard deviation σ_s is the quantity of interest. Since ν determines all statistical moments of the χ^2_ν-distribution it seems to be appealing to investigate the dependency of the variance of the sample standard deviation on the number of degrees of freedom. The variance of the sample standard deviation is given by equation (16):

$$\mathbf{VAR}[\sigma_s] := \mathbf{E}\left[\left(\sigma_s - \mathbf{E}[\sigma_s]\right)^2\right] = \mathbf{E}[\sigma_s^2] - \mathbf{E}[\sigma_s]^2 \,. \tag{16}$$

In order to calculate the expectation values $\mathbf{E}[.]$ in equation (16), the Cochran theorem (17):

$$\mathrm{pdf}\left(\nu \cdot \frac{\sigma_s^2}{\sigma_x^2}\right) = \chi^2_\nu\left(\nu \cdot \frac{\sigma_s^2}{\sigma_x^2}\right) \quad , \quad \text{with:} \quad \sigma_x^2 := \mathbf{VAR}\left[x_i\right] \,, \tag{17}$$

is applied. Here, σ_x^2 characterizes the true variance of the underlying distribution for x_i. Consequently, the expectation value of the sample variance is given by equation (18):

$$\mathbf{E}[\sigma_s^2] := \frac{\sigma_x^2}{\nu} \cdot \mathbf{E}\left[\nu \cdot \frac{\sigma_s^2}{\sigma_x^2}\right] \overset{(17)}{=} \frac{\sigma_x^2}{\nu} \int_0^\infty \xi \; \chi^2_\nu(\xi) \, \mathrm{d}\xi = \sigma_x^2 \,. \tag{18}$$

For the calculation of the expectation value of the sample standard deviation, it is important to recap the relationship for variable changes in pdf's as given by expression (19):

$$\mathbf{E}[\eta := f(\xi)] = \int_{-\infty}^{\infty} \eta \; \mathrm{pdf}_\eta(\eta) \, \mathrm{d}\eta = \int_{-\infty}^{\infty} f(\xi) \; \mathrm{pdf}_\xi(\xi) \, \mathrm{d}\xi \,. \tag{19}$$

As a side note, relation (19) is the mathematical foundation for Monte-Carlo sampling. With this knowledge in mind we can determine the expectation value of the sample standard deviation:

$$\begin{aligned}
&\mathbf{E}[\sigma_s] := \frac{\sigma_x}{\sqrt{\nu}} \cdot \mathbf{E}\left[\sqrt{\nu} \cdot \frac{\sigma_s}{\sigma_x}\right] \overset{(17)}{=} \frac{\sigma_x}{\sqrt{\nu}} \int_0^\infty \eta \; \chi_\nu(\eta) \, \mathrm{d}\eta \\
&\Leftrightarrow \mathbf{E}[\sigma_s] \overset{(19)}{=} \frac{\sigma_x}{\sqrt{\nu}} \int_0^\infty \sqrt{\xi} \; \chi^2_\nu(\xi) \, \mathrm{d}\xi \\
&\Leftrightarrow \mathbf{E}[\sigma_s] = \sqrt{\frac{2}{\nu}} \cdot \frac{\Gamma\left[\dfrac{\nu+1}{2}\right]}{\Gamma\left[\dfrac{\nu}{2}\right]} \cdot \sigma_x \overset{\nu \mapsto \infty}{\longrightarrow} \sigma_x \,.
\end{aligned} \tag{20}$$

Here, Γ denotes the Gamma function [19], which satisfies the relation: $\Gamma[n] = (n-1)!$. In addition, the fact that the square root of residuals of Gaussian distributed observables follows a χ_ν-distribution was used. Finally, the relative standard deviation of the sample standard deviation of x_i is given by equation (21):

$$\begin{aligned}
&\frac{\sigma_{\sigma_s}}{\mathbf{E}[\sigma_s]} = \frac{\sqrt{\mathbf{VAR}[\sigma_s]}}{\mathbf{E}[\sigma_v s]} \overset{(16)}{=} \frac{\sqrt{\mathbf{E}[\sigma_s^2] - \mathbf{E}[\sigma_s]^2}}{\mathbf{E}[\sigma_s]} \overset{(18)}{=} \sqrt{\frac{\sigma_x^2}{\mathbf{E}[\sigma_s]^2} - 1} \\
&\Leftrightarrow \frac{\sigma_{\sigma_s}}{\mathbf{E}[\sigma_s]} \overset{(20)}{=} \sqrt{\frac{\nu}{2} \cdot \frac{\left(\Gamma\left[\dfrac{\nu}{2}\right]\right)^2}{\left(\Gamma\left[\dfrac{\nu+1}{2}\right]\right)^2} - 1} \overset{\nu \mapsto \infty}{\longrightarrow} 0 \\
&\Leftrightarrow \frac{\sigma_{\sigma_s}}{\mathbf{E}[\sigma_s]} = \sqrt{\frac{1}{2\nu}} + \frac{1}{8\sqrt{2}} \cdot \sqrt{\frac{1}{\nu^3}} - \frac{9}{128\sqrt{2}} \cdot \sqrt{\frac{1}{\nu^5}} + \mathcal{O}\left\{\sqrt{\frac{1}{\nu^7}}\right\} .
\end{aligned} \tag{21}$$

In the last line of equation (21), a Puiseux expansion around $\nu \mapsto \infty$ was applied for simplification. A Puiseux series expansion in ν around infinity is loosely speaking a Taylor expansion in ν^{-1} around zero including negative and fractional exponents. By truncating the Puiseux series expansion after first order, the degree of freedom ν of the χ^2_ν-distribution for the estimated sample variance can be determined. Hence, ν can be calculated by equation (22):

$$\nu \overset{(21)}{\approx} \frac{1}{2}\left[\frac{\sigma_{\sigma_s}}{\mathbf{E}[\sigma_s]}\right]^{-2} := \frac{1}{2}\left[\frac{\sigma_s^{(2)}}{\mathbf{E}[\sigma_s]}\right]^{-2} , \tag{22}$$

in accordance with GUM [6]. It is important to emphasize, that relation (22) also holds for the relative standard deviation of the sample standard deviation of the mean μ. This is based on the fact that all expectation values regarding the mean would scale with $\sqrt{N}^{-1}$, wherefore the ratio remains unaffected. Furthermore, equation (22) adapts a slightly different notation for $\sigma_{\sigma_s} := \sigma_s^{(2)}$ in order to indicate the direct link to the second order of uncertainty in x_i. Unfortunately, it is very difficult to give a solid scientific estimate for the second order uncertainty [23]. Therefore, several methods have been published to alleviate this problem for type-B uncertainties, which either draw on the kurtosis [24–26] or perform artificial toy Monte-Carlo studies of independent Bernoulli trials to estimate $\sigma_s^{(2)}$ [27, 28]. For our purpose, the latter method presented by Castrup [27] is adapted for the quantification of $\sigma_s^{(2)}$. As a consequence, the problem of quantifying the second order uncertainty $\sigma_s^{(2)}$ is shifted to the challenge of determining the uncertainty in the confidence level of σ_i. In other words, it has to be estimated how many Bernoulli trials would be sampled within the limits $\pm\sigma_s$, with confidence p, and how many out of distribution subsamples within $\pm\Delta x_i$, with confidence Δp, are observed. Equation (23) approximates the degree of freedom of a type-B uncertainty contribution i, where Φ^{-1} denotes the Gaussian cumulative distribution function.

Table 1. Refractive power measurement uncertainty budget for the laser-based method at $\epsilon = 50°$.

i	x_i	$\langle x_i \rangle$	σ_i	pdf	$\int_{-\sigma_i/2}^{\sigma_i/2} \mathrm{pdf}(\eta)\,\mathrm{d}\eta$	ξ_i	$\frac{\partial D}{\partial x_i}$	u_i	ν_i
1	L	20.65 m	0.02 m	Gaussian	68.3%	1	$-15\,\mathrm{km}^{-1}/\mathrm{m}$	$0.3\,\mathrm{km}^{-1}$	28
2	μ_0	53.0 mm	0.5 mm	Gaussian	68.3%	1	$-5.9\,\mathrm{km}^{-1}/\mathrm{mm}$	$2.95\,\mathrm{km}^{-1}$	28
3	d_c	303.8 mm	0.5 mm	Gaussian	68.3%	1	$0.91\,\mathrm{km}^{-1}/\mathrm{mm}$	$0.46\,\mathrm{km}^{-1}$	28
4	τ_0	38.4 mm	0.5 mm	Gaussian	68.3%	1	$0.91\,\mathrm{km}^{-1}/\mathrm{mm}$	$0.46\,\mathrm{km}^{-1}$	28

$$\nu_i \overset{(22)}{\approx} \frac{1}{2}\left[\frac{u_i^{(2)}}{u_i}\right]^{-2} \overset{!}{=} \frac{1}{2}\left[\frac{\sigma_i^{(2)}}{\sigma_i}\right]^{-2} \overset{[34]}{\approx} \frac{3\sigma_i^2 \cdot \left(\Phi^{-1}\left[\frac{(1+p)}{2}\right]\right)^2}{2\left(\Phi^{-1}\left[\frac{(1+p)}{2}\right]\right)^2 \cdot (\Delta x_i)^2 + \pi\,\sigma_i^2 \cdot \exp\left\{\left(\Phi^{-1}\left[\frac{(1+p)}{2}\right]\right)^2\right\} \cdot (\Delta p)^2} \tag{23}$$

As a side note, the GUM method inherently assumes that the inputted pdf of an observable is not affected by the uncertainty propagation besides the scaling with the sensitivity coefficient, given by the first derivative of the objective function with respect to the observable [29]. As a consequence, the number of degrees of freedom ν is equivalent for σ_i and u_i, where u_i quantifies the projection of the uncertainty contribution σ_i of the input parameter x_i on the objective function u.

For the evaluation of the measurement uncertainty budget presented in table 1, equation (23) was exploited for the calculation of the degrees of freedom of u_i. In detail, the sample standard deviation σ_i on a $p = 68.3\%$ confidence level as well as the estimations for $\Delta x_i = 0.1\sigma_i$ and $\Delta p = 0.1$ were used for the evaluation of ν_i.

3.3.1.2. Measurement uncertainty budget. In table 1, the measurement uncertainty budget for $\epsilon = 50°$ is presented. The input parameters for the determination of the refractive power according to equation (14) are Gaussian distributed, with expectation value $\langle x_i \rangle$ and standard uncertainty σ_i. The estimated variance u_i^2 is $\chi^2_{\nu_i}$-distributed according to Cochran theorem (17) with ν_i degrees of freedom. To estimate the effective variance u^2_{eff}, a linear combination of the input variances u_i^2 is used. At this point it has to be considered that a linear combination of χ^2-distributed variables does not follow an effective χ^2-distribution inherently. Nevertheless, the pdf of u^2_{eff} can be approximated by a new parameterized χ^2-distribution up to the second moment in u^2_{eff}. Hence, the number of degrees of freedom for u^2_{eff} is tuned, so that the expectation value and the variance correspond to the exact solution of the combined distribution given by the convolved u_i^2 distributions. The solution of the equation system is known as the Welch [30]–Satterthwaite [31] equation (24):

$$\nu_{\mathrm{eff}} = \frac{u^4_{\mathrm{eff}}}{\sum_{n=1}^{N} \frac{u_i^4}{\nu_i}}\,. \tag{24}$$

If the effective number of degrees of freedom is large, then the distribution of u^2_{eff} can be approximated as a Gaussian distribution according to the central limit theorem [22]. The Welch–Satterthwaite equation (24) for $\epsilon = 50°$ results in $\nu_{\mathrm{eff}} = 6295$. Hence, the extension factor k for the renormalisation of the confidence intervals can be chosen from a Gaussian pdf. For a confidence level of 95% the extension factor amounts to $k = 1.96$. Consequently, the extended uncertainty u_{ext} on a 95% confidence level for the setup with $\epsilon = 50°$ is given by equation (25):

$$\begin{aligned} u_{\mathrm{ext}} &= k \cdot \sqrt{\sum_{n=1}^{N}\left[\frac{\partial D}{\partial x_i}\cdot\zeta_i\cdot\sigma_i\right]^2} = k \cdot \sqrt{\sum_{n=1}^{N} u_i^2} \\ \Rightarrow u_{\mathrm{ext}} &= \pm\,5.9\,\mathrm{km}^{-1}\quad [95.0\,\%]\,. \end{aligned} \tag{25}$$

For different setups of the inclination angle ε, the extended uncertainty is listed in table 3. For all configurations of ε the effective $\chi^2_{\nu_{\mathrm{eff}}}$-distribution can be approximated as a Gaussian since $\nu_{\mathrm{eff}} > 10$ [32].

4. Comparison measurement

Figure 9 visualizes the deviation of all three measurement techniques from the Kerkhof model. The measurement results from the laser setup are in agreement with the Kerkhof model under consideration of the measurement uncertainties. The same holds for the measurement system that uses Moiré patterns. Nevertheless, the clustering seems to be slightly biased towards larger values of D for the Moiré technique. Finally, the

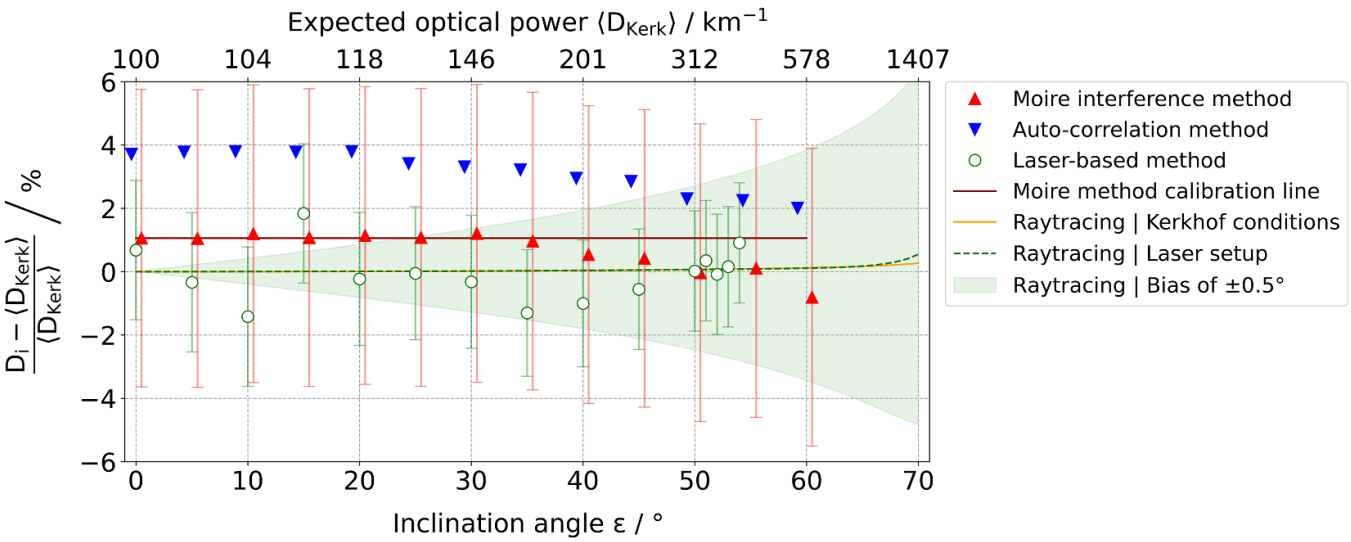

Figure 9. The relative refractive power deviation with respect to the Kerkhof model is plotted versus the inclination angle ϵ for different measurement systems at a 95% confidence level ($k = 1.96$).

auto-correlation method shows the same trend as the expected behaviour by the Kerkhof model. Nevertheless, there is still a significant bias, which is subject to current investigations. Most likely the estimators for the distances of the measurement setup, which enter the refractive power calculation in the matrix optics mapping, are not sufficiently accurate. Hence, the setup alignment procedure has to be refined.

Furthermore, the comparability study baselined on the Kerkhof model indicates that the calibration of the Moire technique is insufficient for refractive powers greater than $\sim 200\,\mathrm{km}^{-1}$. Currently, the measurement device using a Moire interference pattern is calibrated by two reference lenses with $\pm 100\,\mathrm{km}^{-1}$, which are traced back to international standards to ensure a valid calibration chain. The resulting calibration line is assumed to be valid over the entire measurement range. But the results in figure 9 clearly contradict this assumption and indicate that the calibration procedure in place at the moment might be insufficient.

5. The link between refractive power and Fourier optics

In the light of autonomous driving new optical metrics are becoming relevant. Within the ensemble of optical metrics, the MTF plays a central role in assessing the imaging sharpness [33] and is based on the concept of Fourier optics [34]. The dependency of the monochromatic, incoherent $\mathrm{MTF}(\vec{k}|\lambda)$ on the optical path difference $W(\vec{x}_a)$ [34] is determined by equation (26):

$$\mathrm{MTF}(\vec{k}|\lambda) := \left| \frac{\oiint_{P_+ \cap P_-} \exp\left(\frac{2\pi \mathrm{i}}{\lambda}\left[W(\vec{\xi}+\vec{\Delta}) - W(\vec{\xi}-\vec{\Delta})\right]\right) \mathrm{d}\xi^2}{\iint_{\mathbb{R}^2} |P(\vec{\xi})|^2 \,\mathrm{d}\xi^2} \right| ,$$

$$\text{with:} \quad \vec{\Delta} := \lambda z_{a\to o} \frac{\vec{k}}{2} . \tag{26}$$

The integral domain is given by the intersection of the shifted aperture function $P_+ \cap P_-$. Here, the index label indicates the sign of the spatial shift vector $\vec{\Delta}$, which depends on the longitudinal distance between the aperture surface and the observation plane $z_{a\to o}$. The optical path difference W is defined as the difference between the distorted wavefront and the reference wavefront. Concerning the effect of windshield aberrations, the reference wavefront is given by a plane wave. The MTF is a multidimensional function depending on the spatial wavenumber $\vec{k} := (k_x, k_y)$ and the wavelength λ.

If the perturbed wavefront converges locally to a single spot, then the wavefront error can be translated to a local refractive power aberration [35]. In this case, the refractive power D physically quantifies the local curvature of the optical path difference map W [36, 37], as illustrated by equation (27):

$$D_{x_i}(\vec{x}_a) = \frac{\partial^2}{\partial x_i^2} W(\vec{x}_a) . \tag{27}$$

Here, x_i specifies the axis of interest and the input vector $\vec{x}_a \in \mathbb{R}^2$ is bound to the principal plane of the refractive element. Since the information about the wavefront deformation fully characterizes the induced optical aberrations of the windshield it is tempting to investigate if the refractive power is sufficient for reconstructing W, which is attempted by equation (28):

$$\begin{aligned} \triangle W(\vec{x}_a) &\overset{(27)}{=} \sum_{i=1}^{d} D_{x_i}(\vec{x}_a) \\ \Rightarrow W(\vec{x}_a) &= \sum_{i=1}^{d} \left[\oiint_P D_{x_i}(\vec{x}) \cdot G(\vec{x}_a|\vec{x}) \,\mathrm{d}x^2 \right] + \mathcal{C}(\vec{x}_a) \\ \Leftrightarrow W(\vec{x}_a) &:= \sum_{i=1}^{d} \triangle^{-1} D_{x_i}(\vec{x}_a) + \mathcal{C}(\vec{x}_a) \quad , \end{aligned}$$

$$\text{with:} \quad \triangle \mathcal{C}(\vec{x}_a) \overset{!}{=} 0 . \tag{28}$$

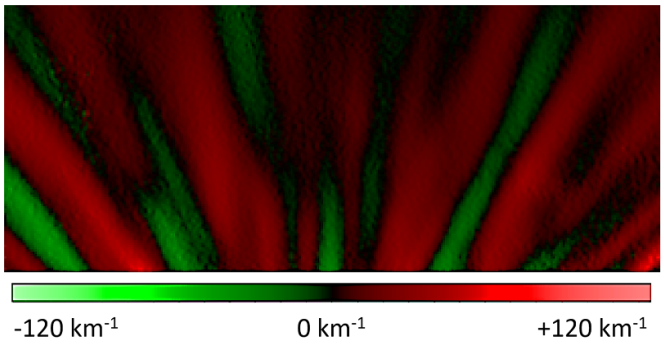

Figure 10. Result of a refractive power measurement of an exemplary windshield in the camera window area.

Here, $G(\vec{x}_a|\vec{x})$ denotes the Green's function for the two-dimensional Laplacian on $\mathbb{R}^2$ given by equation (29) [38]:

$$G(\vec{x}_a|\vec{x}) = \frac{1}{2\pi}\ln\left(\|\vec{x}-\vec{x}_a\|_2\right). \tag{29}$$

Equation (28) demonstrates that the wavefront aberration map could be reconstructed on the basis of refractive power measurements if two conditions are fulfilled. First of all, the resolution of the refractive power measurement has to be sufficiently high in order to numerically calculate the integral. Secondly, the integration constant $\mathcal{C}(\vec{x}_a)$ in equation (28), which necessarily fulfills the Laplace equation, has to be negligible over the entire aperture. Hence, all aberration fields that can be decomposed into harmonic functions are not recoverable by the inversion of the refractive power distribution. The latter condition is most likely not fulfilled in general for the aberration structure induced by windshields. This indicates the insufficiency of refractive power measurements for safeguarding autonomous driving because the link to the MTF is limited by the inversion information loss [35].

Nonetheless, high-resolution refractive power measurements are desirable for quantifying optical distortions within the ADAS camera area, which can be utilized to ensure a rectilinear mapping in the perception system by post-processing. For this purpose, it is of paramount importance to consider the dependency of the distortion magnitude on the field of view. This is most likely the unique selling point of the measuring technique presented in section 3.2 because it inherently takes care of this reliance. As an example, figure 10 visualizes the refractive power distribution on the aperture surface for a given car imaging system. It has to be emphasized, that there is a non-zero refractive power gradient in the vertical as well as in the horizontal direction reflecting the varying angle of field, which ultimately amplifies the refractive power according to the Kerkhof model.

Table 2. Table of specifications for the setups involved in the comparability study regarding different refractive power measurement techniques.

Method	Accuracy	Resolution	Practicability
Moiré method	○	○	●
Auto-correlation method	○	●	●
Laser-based method	●	●	●

6. Benefits and outlook

In a nutshell, the comparability of different measuring techniques regarding the refractive power has been demonstrated and a calibration procedure has been proposed, which can be utilized to ensure the traceability of the measurement results to international metrological reference standards. The specifications of the investigated measurement setups are compared in table 2. As a next step, a detailed analysis has to be undertaken, which aims for investigating the non-zero bias of the auto-correlation measurement method. As soon as this puzzle is resolved, high-resolution refractive power maps from windshield measurements can be utilized to ensure a rectilinear mapping in the perception system and thereby contribute to the fulfillment of the performance requirements for level 4 ADAS functionalities.

Appendix and data availability statement

In general, any data that support the findings of this study are included within the article. Table 3 lists the refractive power measurement results obtained by the laser-based method. Here, δD labels the relative deviation of the measurement from the expectation value predicted by the Kerkhof model (12). Furthermore, the sensitivity coefficients—namely the local partial derivatives of the objective function (14) with respect to the observable parameter of interest—are stated explicitly. In addition, the effective measurement uncertainty u_{eff} as well as the effective number of degrees of freedom ν_{eff} is provided for each measuring point.

Table 3. Measurement data obtained by the laser-based method w.r.t. a reference lens from Carl Zeiss AG with $\langle \mathrm{D}_{\epsilon=0^\circ} \rangle = 100.25\,\mathrm{km}^{-1}$ as the object under test.

ϵ/ ○	d_c/ mm	$\mathrm{D_{eff}}$/ km^{-1}	$\mathrm{D_{Kerk}}$/ km^{-1}	$\delta\mathrm{D}$/ %	$\partial_L\mathrm{D}$/ m^{-2}	$\partial_{\mu_0}\mathrm{D}$/ m^{-2}	$\partial_{d_c}\mathrm{D}$/ m^{-2}	$\partial_{\tau_0}\mathrm{D}$/ m^{-2}	u_{eff}/ km^{-1}	ν_{eff}/ 1	k/ 1	u_{ext}/ km^{-1}	$u_{\mathrm{ext}}\mathrm{D}_{\mathrm{eff}}^{-1}$/ %
0	71.8	101	100.3	0.4	−0.005	−1.9	0.91	0.91	1.2	54	1.96	2.3	2.2
5	72.2	101	101.3	−0.3	−0.005	−1.9	0.91	0.91	1.2	54	1.96	2.3	2.2
10	74.4	103	104.5	−1.4	−0.005	−1.9	0.91	0.91	1.2	53	1.96	2.3	2.2
15	84.1	112	110.0	1.8	−0.005	−2.1	0.91	0.91	1.2	50	1.96	2.4	2.2
20	90.7	118	118.3	−0.3	−0.006	−2.2	0.91	0.91	1.3	48	1.96	2.5	2.1
25	104.2	130	130.1	0.2	−0.006	−2.5	0.91	0.91	1.4	44	1.96	2.7	2.1
30	121.5	146	146.5	−0.2	−0.007	−2.8	0.91	0.91	1.5	41	1.96	3.0	2.1
35	144.7	167	169.2	−1.1	−0.008	−3.2	0.91	0.91	1.7	38	1.96	3.4	2.0
40	179.7	199	201.0	−0.9	−0.010	−3.8	0.91	0.91	2.0	35	1.96	3.9	2.0
45	230.1	245	246.4	−0.4	−0.012	−4.6	0.91	0.91	2.4	33	1.96	4.7	1.9
50	303.8	313	312.9	−0.1	−0.015	−5.9	0.91	0.91	3.0	31	1.96	5.9	1.9
51	324	331.0	329.9	0.4	−0.016	−6.2	0.91	0.91	3.2	31	1.96	6.3	1.9
52	342.8	348	348.3	0.0	−0.017	−6.6	0.91	0.91	3.4	30	1.96	6.6	1.9
53	365.9	369	368.4	0.3	−0.018	−7.0	0.91	0.91	3.6	30	1.96	7.0	1.9
54	392.5	394	390.4	0.8	−0.019	−7.4	0.91	0.91	3.8	30	1.96	7.4	1.9

ORCID iDs

Dominik Werner Wolf https://orcid.org/0000-0002-6631-3312
Markus Ulrich https://orcid.org/0000-0001-8457-5554
Alexander Braun https://orcid.org/0000-0002-8358-0578

References

[1] SAE International Standard J3016-202104 2021 Taxonomy and definitions for terms related to driving automation systems for on-road motor vehicles (available at: www.sae.org/standards/content/j3016_202104/)
[2] Gupta S *et al* 2023 Far3Det: towards far-field 3D detection *IEEE/CVF Winter Conf. on Applications of Computer Vision* (*WACV*) (*USA*) pp 692–701
[3] Mitra T 2022 White paper on the benefits of optical distortion measurement *ISRA Vision* (available at: www.vdma.org/documents/34570/4887360/11+Benefits+of+optical+distortion+measurement+202207.pdf/d2dfc5af-c373-248c-db5c-deaa1b01026d?t = 1659424930528)
[4] DIN-52305, German Institute for Standardization 1995 Determination of the optical deviation and refractive power of safety glass for vehicle glazing *Entry into force on June 1995* (available at: www.beuth.de/de/norm/din-52305/2533097)
[5] LaVision GmbH Background oriented schlieren: BOS imaging, Göttingen, Germany (available at: http://digitalimagecorrelation.com/de/techniques/schlieren-bos/index.php)
[6] Joint Committee for Guides in Metrology (JCGM) 2008 Evaluation of measurement data - Guide to the expression of uncertainty in measurement (GUM) *International Bureau of Weights and Measures* (*BIPM*) (*Sèvres, France*) (available at: www.bipm.org/documents/20126/2071204/JCGM_100_2008_E.pdf/cb0ef43f-baa5-11cf-3f85-4dcd86f77bd6)
[7] Kerkhof F 1952 Optische Wirkungen von Flachglas mit unebenen Oberflächen *Glastechnische Berichte* **25** 71–83 (available at: www.tib.eu/en/search/id/ei-backfile:c84_f4ab65fd80746efdM7a0719817173212/Optical-effects-of-flat-glass-with-uneven-surfaces?cHash = 396abec3815801caf47fb55f77b43461)
[8] Schardin H and Stamm G 1942 Ballistic Institute of the aerial warfare academy in Berlin. Prüfung von Flachglas mit Hilfe eines farbigen Schlierenverfahrens. *Glastechnische Berichte* **20**
[9] ISRA VISION GmbH, LABSCAN-SCREEN Fortschrittliches Offline-System für hochauflösende Messergebnisse, Darmstadt, Germany (available at: www.isravision.com/de/flat-panel-display-glas/anwendungen/floatglas-fuer-duennglas/labscan-screen/)
[10] Goto H 2009 Moiré patterns allow us to visualize the interference between propagating waves *Phys. Educ.* **44** 338
[11] Indebetouw G and Czarnek R 1992 *Selected Papers on Optical Moiré and Applications* (SPIE Optical Engineering Press)
[12] Raffel M 2015 Background-oriented schlieren (BOS) techniques *Exp. Fluids* **56** 60
[13] Bichal A and Thurow B S 2013 On the application of background oriented schlieren for wavefront sensing *Meas. Sci. Technol.* **25** 015001
[14] Ek S, Kornienko V, Roth A , Berrocal E and Kristensson E 2022 High-speed videography of transparent media using illumination-based multiplexed schlieren *Nat. Sci. Rep.* **12** 19018
[15] Regulation No. 43 of the Economic Commission for Europe of the United Nations (UN/ECE) - Uniform provisions concerning the approval of safety glazing materials and their installation on vehicles *Official Journal of the European Union 31 August 2010*
[16] Schwarz W 2020 Methods for the determination of the measurement uncertainty using GUM - Part 1, avn, vol. 127, no. 2, p. 69–86 (available at: www.gik.kit.edu/downloads/%5BSCHW20%5DGUM_AVN_Teil1.pdf)
[17] Knight K 2000 *Mathematical Statistics* (Chapman and Hall/CRC Press)
[18] BOX G E P, Gordon HUNTER W and Stuart HUNTER J 1978 *Statistics for Experimenters: an Introduction to Design, Data Analysis and Model Building* (*Wiley Series in Probability and Mathematical Statistics*) (Wiley)
[19] Upton G and Cook I 2008 *A Dictionary of Statistics* (Oxford University Press)
[20] Taboga M 2021 Ridge regression', Lectures on probability theory and mathematical statistics. Kindle Direct Publishing *Online appendix* (available at: www.statlect.com/fundamentals-of-statistics/ridge-regression)
[21] Shmueli G, Bruce P C, Yahav I, Patel N R and Lichtendahl K C 2018 *Data Mining for Business Analytics: Concepts, Techniques and Applications in R* (Wiley)

[22] Stroock D W 2010 Massachusetts Institute of Technology. The Central Limit Theorem *Probability Theory: An Analytic View* (Cambridge University Press) pp 59–114
[23] Farrance I and Frenkel R 2012 Uncertainty of measurement: a review of the rules for calculating uncertainty components through functional relationships *Clin. Biochem. Rev.* **33** 49–75 (available at: https://pubmed.ncbi.nlm.nih.gov/22896744/)
[24] Willink R 2022 An enhanced method for the evaluation of measurement uncertainty *Meas. Sens.* **24** 100373
[25] Willink R 2021 An accurate and consistent procedure for the evaluation of measurement uncertainty *Meas. Sens.* **18** 100334
[26] Ames M H and Webster J T 1991 On estimating approximate degrees of freedom *Am. Statistician* **45** 45–50
[27] Castrup H T 2000 Estimating category B degrees of freedom *Proc. Measurement Science Conf.* (available at: http://download.caltech.se/download/validering/diverse/uncert/Degrees_of_Freedom.pdf)
[28] Castrup H T 2001 Estimating bias uncertainty *Proc. NCSLI Workshop and Symp.* (available at: www.isgmax.com/Articles_Papers/Estimating%20Bias%20Uncertainty.pdf)
[29] Schwarz W 2020 Methods for the determination of the measurement uncertainty using GUM - Part 2, avn, vol. 127, no. 5, p. 211–219 (available at: www.gik.kit.edu/downloads/%5BSCHW20%5DGUM_AVN_Teil2.pdf)
[30] Welch B L 1947 The generalization of student's problem when several different population variances are involved *Biometrics Bulletin* **34** 28–35
[31] Satterthwaite F E 1946 An approximate distribution of estimates of variance components *Biometrics Bulletin* **2** 110–4
[32] Pesch B 2003 *Bestimmung der Messunsicherheit Nach GUM, Grundlagen der Metrologie* (B. Pesch)
[33] Weikla K, Frisvadc J R, Schroeder D and Stechelea W 2022 Imaging through curved glass: windshield optical impact on automotive cameras *Proc. SPIE* **12231** 122310A
[34] Goodman J W and University S 1968 *Introduction to Fourier Optics* (McGraw-Hill)
[35] Wolf D W, Ulrich M and Braun A 2023 Windscreen optical quality for AI algorithms: refractive power and MTF not sufficient (arXiv:2305.14513)
[36] Thibos L N 2019 Calculation of the geometrical point-spread function from wavefront aberrations *Ophthalmic Physiol. Opt.* **39** 232–44
[37] Thibos L N, Hong X, Bradley A and Applegate R A 2004 Accuracy and precision of objective refraction from wavefront aberrations *J. Vis.* **4** 9
[38] Kythe P K 2011 *Green's Functions and Linear Differential Equations: Theory, Applications and Computation* (CRC Press)